

# Introducing Hysteresis in Snow Depletion Curves to Improve the Water Budget of a Land Surface Model in an Alpine Catchment

CLAIRE MAGAND, AGNÈS DUCHARNE, AND NICOLAS LE MOINE

*UMR Sisyphe, UPMC/CNRS, Paris, France*

SIMON GASCOIN

*CESBIO, Toulouse, France*

(Manuscript received 21 May 2013, in final form 1 October 2013)

## ABSTRACT

The Durance watershed (14 000 km<sup>2</sup>), located in the French Alps, generates 10% of French hydropower and provides drinking water to 3 million people. The Catchment land surface model (CLSM), a distributed land surface model (LSM) with a multilayer, physically based snow model, has been applied in the upstream part of this watershed, where snowfall accounts for 50% of the precipitation. The CLSM subdivides the upper Durance watershed, where elevations range from 800 to 4000 m within 3580 km<sup>2</sup>, into elementary catchments with an average area of 500 km<sup>2</sup>. The authors first show the difference between the dynamics of the accumulation and ablation of the snow cover using Moderate Resolution Imaging Spectroradiometer (MODIS) images and snow-depth measurements. The extent of snow cover increases faster during accumulation than during ablation because melting occurs at preferential locations. This difference corresponds to the presence of a hysteresis in the snow-cover depletion curve of these catchments, and the CLSM was adapted by implementing such a hysteresis in the snow-cover depletion curve of the model. Different simulations were performed to assess the influence of the parameterizations on the water budget and the evolution of the extent of the snow cover. Using six gauging stations, the authors demonstrate that introducing a hysteresis in the snow-cover depletion curve improves melting dynamics. They conclude that their adaptation of the CLSM contributes to a better representation of snowpack dynamics in an LSM that enables mountainous catchments to be modeled for impact studies such as those of climate change.

## 1. Introduction

A strong positive feedback on climate comes from the surface albedo, especially over snow-covered areas characterized by a high reflectivity. Snow cover is also responsible for the strong seasonal contrasts observed in the hydrological regimes of mountainous and high-latitude regions. During winter, snow cover acts as a water reservoir where snowfall accumulates. A large quantity of water is subsequently released during the melt season. Modeling snow cover is therefore crucial for accurate simulation of both the energy and water budgets.

During the last three decades, major efforts have been made by the land surface model (LSM) community to

better describe snowpack physics by increasing vertical resolution and complexifying snow parameterizations. Such improvements led to better ground thermodynamics at the continental scale (Loth and Graf 1998; Stieglitz et al. 2001), but difficulties in simulating the timing of snowpack ablation remained (Pomeroy et al. 1998; Slater et al. 2001). Accounting for the subgrid variability of the snow-cover extent is important because it modifies the energy and water budgets via its effect on the mean albedo, but also because it changes the dynamics of fluxes related to the presence of snow on the grid cell (e.g., sublimation and melt). Many snow-cover depletion curves (SCDs) relating the snow-cover fraction (SCF) of a grid cell to the average snow depth or snow water equivalent (SWE) were introduced to account for the horizontal variability of the snow cover within an LSM's grid cell (Gray and Male 1981; Hansen et al. 1983; Verseghy 1991; Douville et al. 1995; Yang et al. 1997; Roesch et al. 2001; Essery and Pomeroy 2004). The

---

*Corresponding author address:* Claire Magand, UMR Sisyphe, CNRS/UPMC Paris 6, 4 Place Jussieu, 75252 Paris CEDEX 05, France.

E-mail: [claire.magand@upmc.fr](mailto:claire.magand@upmc.fr)

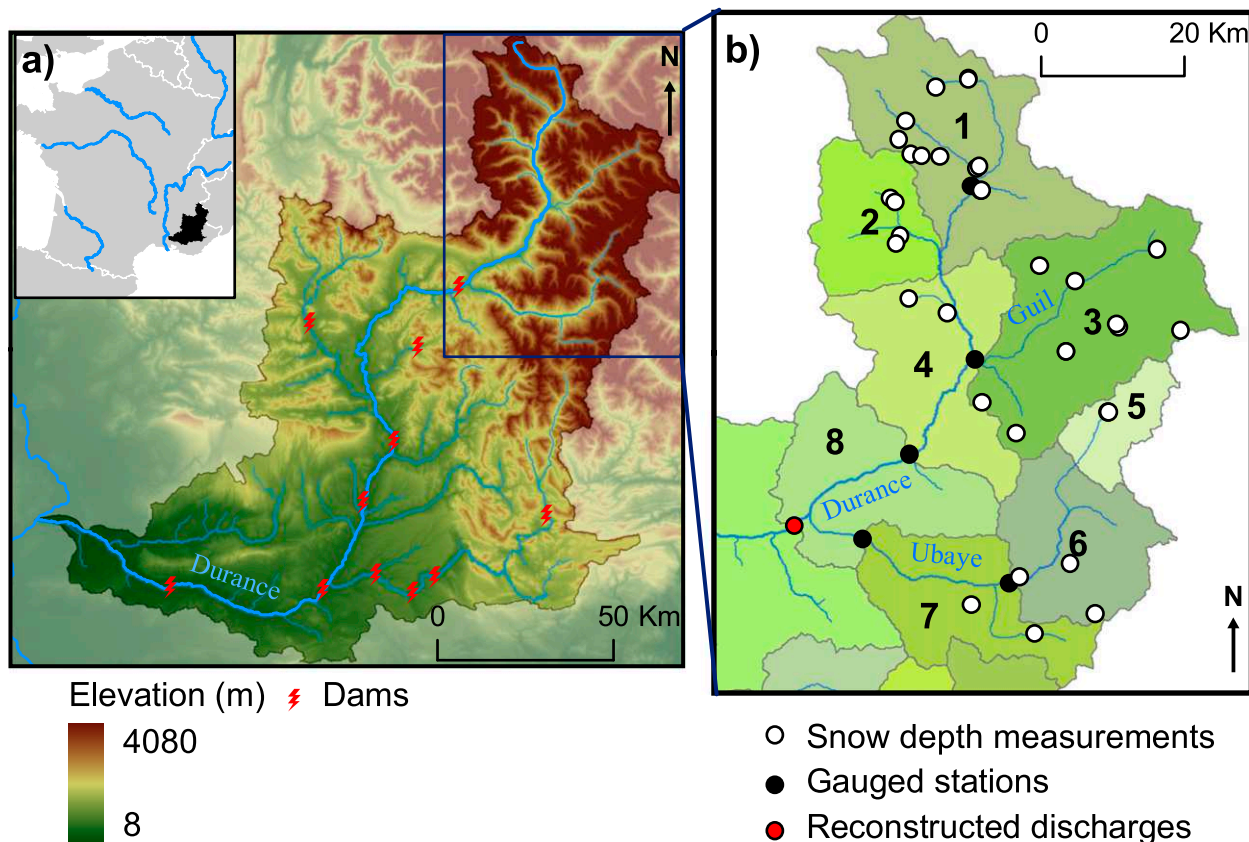


FIG. 1. (a) Durance watershed elevations and dam locations. (b) Upper part of the Durance watershed with delineation of elementary catchments used in the CLSM and locations of the gauging stations and snow depth measurements.

sophistication of these SCDs has increased over the years, from a linear equation limited by an SWE threshold (Verseghy 1991; Sellers et al. 1996) applied to all types of vegetation to more complex algorithms accounting for vegetation properties, wind effects, or ground roughness length (Déry et al. 2004; Livneh et al. 2010; Wang 2012).

At a small scale (26 ha), Luce and Tarboton (2004) highlighted the existence of a hysteresis in the SCD with different dynamics between accumulation and ablation periods. During accumulation, the snow-cover extent quickly reaches full coverage, after which the snowpack increases homogeneously in depth. In contrast, snow melts from preferential locations during ablation, leading to heterogeneous patterns. Liston (2004) also developed a subgrid snow distribution to describe these two different processes and validated this method at the mesoscale (2500 km<sup>2</sup>). More recently, Niu and Yang (2007) and Dutra et al. (2010) introduced a hysteresis in the SCD by inversely relating the snow-cover area to the snowpack bulk density: as the snow density increases with respect to the snow age, the snow-cover area for a given quantity of snow gets lower later in the snow season. Although this study showed good consistency with satellite images of

snow cover at a global scale (10 000 km<sup>2</sup>), we concur with Swenson and Lawrence (2012) that the observed hysteresis is more likely due to the variability of topography or vegetation within the catchment than to the age of snow.

The Catchment land surface model (CLSM) is an LSM developed by Koster et al. (2000) and Ducharme et al. (2000) to generate water and energy fluxes between land surfaces and the atmosphere in general circulation models (GCMs) in which a multilayer, physically based snow scheme is included (Lynch-Stieglitz 1994). We applied this model in the Durance watershed (approximately 14 000 km<sup>2</sup>) located in the southern French Alps with an altitude range of 4000 m (see Fig. 1). We focus on the upper catchment part, which provides 40% of the discharge at the outlet of the Durance watershed and where snowfall accounts for more than 50% of the total precipitation. A correct estimation of the water resource and its evolution under climate change is particularly important as 10% of French hydropower is produced in the Durance watershed (Fig. 1) and it supplies drinking water to approximately 3 million people.

The CLSM subdivides the domain into elementary catchments, here with an average area of 500 km<sup>2</sup>

TABLE 1. Characteristics of each elementary catchment in the upper Durance River (UDR) watershed. There are six gauging stations in the upper Durance watershed. U.A.S. is the upstream area at the gauging station and  $\overline{Q}_{\text{obs}}$  is the mean observed discharge. The SD stations are stations of snow-depth measurements and  $W_{\text{melt}}$  is the parameter introduced to create the hysteresis in the snow cover depletion curve.

Catchment ID	Area (km <sup>2</sup> )	U.A.S. (km <sup>2</sup> )	$\overline{Q}_{\text{obs}}$ (m s <sup>-3</sup> )	Number of SD stations	Elevation (m)		Land cover fraction (%)			$W_{\text{melt}}$ (kg m <sup>-1</sup> )
					Mean	Range	Forest	Grass	Bare soil	
1	662	548	13.0	12	2133	2675	23	32	45	400
2	296	—	—	4	2267	3125	17	31	53	400
3	723	723	11.6	10	2176	2465	29	37	34	300
4	501	2170	49.4	2	1880	2427	31	37	32	100
5	147	—	—	2	2539	1894	6	34	60	500
6	397	549	9.7	3	2093	2021	22	38	40	400
7	401	946	19.5	2	1902	2238	37	30	33	13
8	461	3582	76.3	—	1511	2215	35	45	20	13
UDR	3588	3582	76.3	35	2024	3298	37	36	27	—

(Fig. 1b). Topography, vegetation, and aspect (north facing or south facing) are highly variable within each elementary catchment in the upper Durance watershed, and these three features play a key role in producing heterogeneous snow cover, especially during melting events (Gray and Male 1981; Lundberg et al. 1998; Essery and Pomeroy 2004; Liston 2004; Swenson and Lawrence 2012). Hence, the extent of the snow cover should vary within each catchment and impact the time and rate of melt. Therefore, the objectives of this study were first to investigate whether or not there is a hysteresis in the observed relationship between SCF and SWE using Moderate Resolution Imaging Spectroradiometer (MODIS) images and snow-depth measurements and then to assess the influence of the SCF parameterizations on the simulated water budget in the context of an Alpine environment.

## 2. Characterization of the observed hysteresis

The upper Durance River watershed was subdivided into eight elementary catchments of about 500 km<sup>2</sup> for the requirements of the model (section 3). A 25-m digital elevation model (DEM) produced by the French National Geographic Institute (IGN) was used to delineate the catchments. Accounting for the locations of the gauging stations was also important to delineate the catchments so that the simulations could be validated with observations. Eventually, lithological data from the French Geological Survey (BRGM) were collected to ensure that hydrological catchments were homogeneous in terms of soil characteristics. Table 1 summarizes the characteristics of each catchment.

### a. Snow-cover area and snow-depth datasets

SCFs were calculated from mid-resolution images of snow-cover extent provided by MOD10A2 (see [http://nsidc.org/data/docs/daac/modis\\_v5/mod10a2\\_modis\\_terra\\_snow\\_8-day\\_global\\_500m\\_grid.gd.html](http://nsidc.org/data/docs/daac/modis_v5/mod10a2_modis_terra_snow_8-day_global_500m_grid.gd.html)), an 8-day

composite snow product from MODIS. Snow-cover and cloud-cover extents are given as binary information in 500-m pixels from April 2000 to February 2012. A pixel is labeled as “snow covered” if snow was observed at least once; a pixel is labeled as clouded if the cell was obscured by clouds during all observation days (Riggs et al. 2006). The SCF and cloud-cover fraction of each catchment were extracted from these images using GIS tools. Cloud cover can significantly reduce snow-cover extent measurements. Therefore, we excluded images where 10% of the catchment was cloud covered, which corresponded to 6% of each time series. Note also that the SCFs of catchment 2 were not taken into account in this study because MODIS SCFs seem to overestimate the snow-cover area in this catchment (indicating snow even in summer), most likely because of the presence of glaciers (approximately 20% of the catchment area). We did not consider MODIS observations on a daily time scale as previous studies have demonstrated that approximately 60% of the images are obscured by clouds in the Alps (Parajka and Blöschl 2006; Picouet 2012).

To characterize the empirical SCD, snow-depth data were also collected from the Base de Données Climatologiques (BDCLIM), a dataset produced by Météo-France, the French national weather service. Snow-depth measurements were obtained from 89 stations located in the upper Durance. Most of these stations, however, do not provide useful information because there are too many gaps, and so we used only 35 stations providing measurements between April 2000 and March 2006 (Fig. 1). The number of stations used in each catchment is indicated in Table 1. In catchments 1, 3, and 6, the elevation of these stations is well distributed within the elevation range of the catchment to which they belong (Fig. 1). We mainly show results from catchment 3 in this article because it is the best instrumented with 10 stations, the elevations of which range from 1355 to 2630 m, while catchment elevations range from 892 to 3357 m. This is not the case in the other

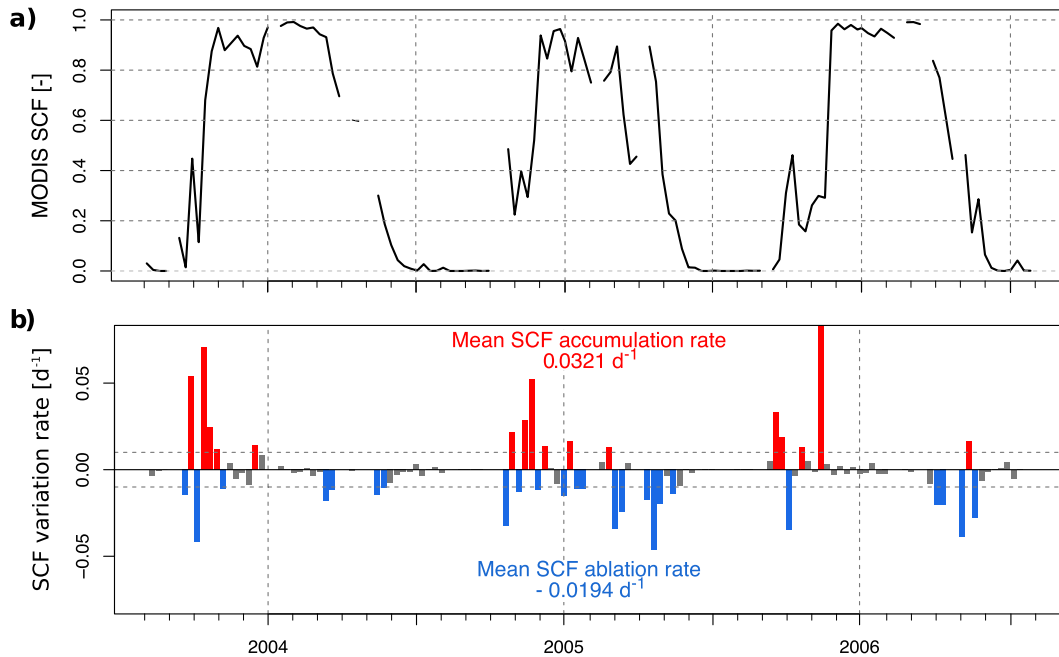


FIG. 2. (a) SCF time series extracted from MODIS images (MOD10A2) in catchment 3 from July 2003 to August 2006. Interruptions reflect weeks when cloud cover was  $>10\%$ . (b) Rates of SCF ( $\text{day}^{-1}$ ) with accumulation represented by red bars and ablation by blue bars calculated over 2000–11. Rates  $< 0.01 \text{ day}^{-1}$  in absolute terms (gray) are considered to be neutral and are not used in calculating the means. Taking them into account does not change our overall conclusion.

catchments, where the stations are located around the same elevation. In catchment 4 for instance, there are only two stations gathered along the streams, both being at an elevation of about 1200 m (Fig. 1). Snow-depth measurements were averaged over each catchment to get a mean snow-depth time series. The consequences of this averaging in catchments where the snow-depth stations are not representative are discussed in the following section.

### b. Revealing the hysteresis

The snow season usually starts at the beginning of October in the upper Durance watershed and ends at the beginning of June, as illustrated for catchment 3 in Fig. 2a. More than 80% of the catchment area is covered with snow for more than 5 months. From these SCF time series, rates of SCF ( $\Delta\text{SCF}/\Delta t$ ) were calculated and are displayed in Fig. 2b. This graph reveals clear differences in snow-cover dynamics between accumulation and ablation events. The mean accumulation rate is 1.7 higher than the mean ablation rate, which means that the SCF increases faster than it decreases. This difference of variation rate strongly suggests the existence of a hysteresis in the SCD, as described by Luce et al. (1999).

Figure 3 shows, using snow-depth measurements, a hysteresis in the SCD of catchment 3. This hysteresis was also observed in catchments 1 and 6, but not in the other elementary catchments. This is likely because the

point data in these catchments were not representative of the mean snow depth, as explained in section 2a.

As suggested above, the hysteresis exists because the variables in the SCD, snow depths, and SCFs, are aggregated over the catchment and their values can represent

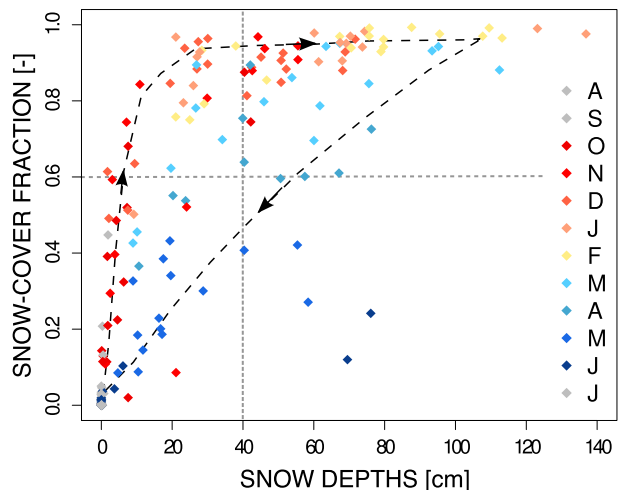


FIG. 3. MODIS SCF vs maximum mean snow-depth observations in catchment 3 over 8 days from April 2000 to March 2006. Reddish colors represent months when snow-cover accumulation prevails and bluish colors when snow-cover ablation is most important. Neutral colors such as gray and beige represent months with either no snow or very little change in the snow-cover extent.

different internal states of the aggregated snowpack of the catchment. For example, if we consider a mean snow depth of 40 cm, the SCF could be equal to 100% or to 40%. Reciprocally, if we consider an SCF equal to 60%, the mean snow depth could be equal to 5 or 60 cm. In addition, the configuration of the snowpack is not random in time. Figure 3 shows that from October to December, the snow-cover extent of the catchment increases quickly with a small amount of snow. Then the SCF remains constant along the horizontal asymptote of full snow coverage from December to February while snow depth increases to its maximum value. Eventually, from March to June, a gradual reduction of the SCF occurs as the mean snow depth decreases. This time pattern is due to the differences between the two processes of accumulation and ablation. During accumulation, snowfall tends to spread uniformly all over the catchment. By contrast, melting occurs in preferential locations. Snow stays longer at high elevations, over north-facing slopes, and in small hollows created by terrain heterogeneities. Vegetation and windblown effect can also influence ablation of the snowpack (Gray and Male 1981; Lundberg et al. 1998; Essery and Pomeroy 2004). As a result, the high variability of topography and vegetation in each catchment (Table 1) explains the hysteresis illustrated in Fig. 3.

Consequently, the knowledge of a single characteristic of the aggregated snowpack, either SWE or SCF, is not sufficient to describe its spatial setting. The subgrid variability of the catchment must be accurately defined to predict the future development of the snowpack, which can be achieved by (i) using a finer discretization (Lafaysse 2011), (ii) using a subgrid probability function, or (iii) accounting for the history of the snowpack by means of a hysteresis parameterization (Mielke and Roubicek 2003). In the latter case, lack of spatial information is thus compensated by historical information.

Although the hysteresis could not be observed in all elementary catchments, differences between SCF accumulation and ablation rates are confirmed for all of them (Fig. 4). Whereas ablation SCF rates are gathered close to zero, accumulation SCF rates are spread over a larger range of values, and the mean accumulation rate is 1.65 times higher than the ablation rate. From this result and those found in catchments 1, 3, and 6, we assume that this hysteresis exists in every elementary catchment of the upper Durance watershed.

### 3. Modeling concepts

#### a. General principles

As a land surface model, the CLSM (Koster et al. 2000; Ducharme et al. 2000) is designed to simulate the

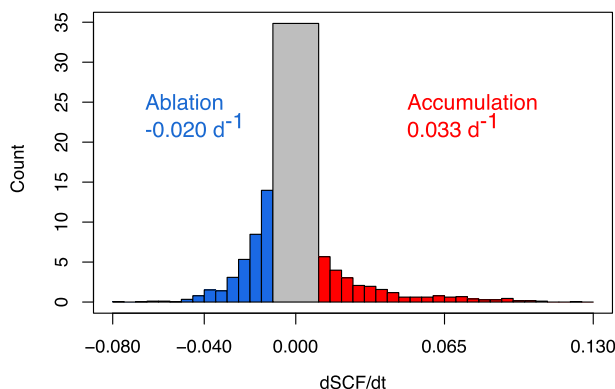


FIG. 4. Histogram of observed SCF variation rates derived from MODIS images for the entire upper Durance catchment. Mean accumulation and ablation rates (red and blue, respectively) are calculated over 2000–11. The central bin, corresponding to small absolute variation rates ( $<0.01 \text{ day}^{-1}$ ), is in gray and not used to calculate the mean rates of accumulation or ablation. These small rates are not significant given the accuracy of MODIS images and retaining them does not change the difference between the two mean rates.

diurnal cycle of land surface water and energy fluxes as a function of near-surface meteorology (precipitation, shortwave and longwave incident radiation, surface pressure, air temperature and humidity at 2 m, and wind speed at 10 m); it can be either be coupled to a GCM or used offline, as in this present study. A characteristic of this LSM is to relate subgrid soil moisture heterogeneities with topography using TOPMODEL concepts (Beven and Kirkby 1979). The topographic index is a soil moisture indicator and is formulated as follows:

$$x = \ln(a/\tan\beta), \quad (1)$$

where  $a$  is the upslope contributing area per unit contour length and  $\tan\beta$  is the local topographic slope. High values of the topographic index denote low land easily liable to saturation, whereas low values result from small drainage areas and steep slopes, characteristic of mountain ridges.

Hydrological catchments are used as the fundamental land surface element, and horizontal soil moisture variability within each catchment is described on the basis of the topographic index distribution. This resulting distribution of soil moisture allows partitioning into three areal fractions with distinct hydrological functioning: stressed, intermediate, and saturated (e.g., no evapotranspiration takes place from the stressed fraction). These fractions vary in time as a result of the catchment water budget, with an increased stressed fraction in dry periods and an increased saturated fraction in wet periods. Fluxes, such as evapotranspiration or runoff, are described using classic soil–vegetation–atmosphere

transfer (SVAT) formulations, mostly taken from the Mosaic LSM (Koster and Suarez 1996).

### b. Description of the subgrid variability of vegetation

Eight classes of vegetation are defined in the CLSM, and proportions of each were extracted from ECOCLIMAP, a global database of land surface parameters at 1-km resolution (Masson et al. 2003). The vegetation classes are summarized into three main types of land cover in Table 1, which shows that different types of vegetation coexist in similar proportions. They have very distinct properties [leaf area index (LAI), albedo, etc.] and are likely to play a key role in the subgrid variability of the snow-cover extent illustrated in Fig. 3. We thus decided to allow a mosaic of vegetation types, in contrast to the latest studies (Koster et al. 2000; Ducharne et al. 2000; Stieglitz et al. 2001; Déry et al. 2004; Gascoin et al. 2009b), which assumed that the catchment was uniformly covered with the dominant vegetation. The resulting vegetation “tiles” share the same soil moisture variables, but they have independent energy budgets and the snow model is applied to each vegetation tile. We refer to this configuration of the CLSM as multitile in the following sections.

### c. Initial snow-cover parameterization

The multilayer, physically based snow scheme included in the CLSM (Lynch-Stieglitz 1994) is of intermediate complexity according to Boone and Etchevers’s (2001) classification of snow schemes and has shown good performance in different studies (Stieglitz et al. 2001; Gascoin et al. 2009b; Koster et al. 2010). The snow model vertically discretizes the snowpack into three layers, and each of them is characterized by its heat content, SWE, and snow depth (Lynch-Stieglitz 1994; Stieglitz et al. 2001; Déry et al. 2004). As detailed in Lynch-Stieglitz (1994), these variables vary in time by means of three processes:

- heat transfer between the atmosphere and the snowpack surface layer (sublimation, condensation, or sensible heat flux) and between each layer (thermal diffusion);
- mass transfer between the atmosphere and the snowpack surface layer (precipitation) and between the layers (meltwater); and
- snow compaction in each layer.

A threshold of SWE,  $W_{\min}$  of  $13 \text{ kg m}^{-2}$ , was set to ensure a smooth transition between snow-free and snow-covered conditions. When the SWE is less than  $W_{\min}$ , the SCF of the catchment  $F$  is defined as follows:

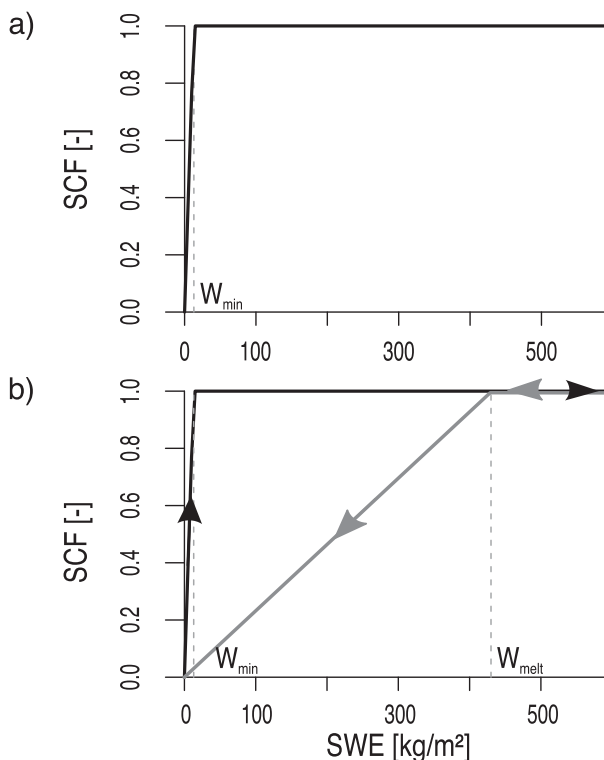


FIG. 5. (a) Initial snow-cover depletion curve of the CLSM. (b) New snow-cover depletion curve with hysteresis. The path taken by the SCF with respect to SWE is shown in black for accumulation and in gray for ablation.

$$F = \begin{cases} \frac{W}{W_{\min}} & \text{if } W < W_{\min} \\ 1 & \text{if } W \geq W_{\min} \end{cases}, \quad (2)$$

where  $W$  is the snow water equivalent ( $\text{kg m}^{-2}$ ) of the catchment. Figure 5a displays the initial SCD. Once the SWE reaches  $W_{\min}$  and stays above this value, the SCF is equal to 1 and the snowpack grows vertically rather than horizontally. The snow cover is assumed to remain spatially uniform across the catchment, with depth being spatially constant.

### d. New snow-cover depletion curve with hysteresis

Aspect and slope also play a significant role during the melt (Liston 2004), and accounting for the subgrid variability of vegetation may not be enough to reproduce the hysteresis demonstrated in section 2. Therefore, we decided to introduce a hysteresis in the initial SCD using a new parameter,  $W_{\text{melt}}$ . During accumulation, the SCF quickly increases with initial snowfall, and the relationship between the SCF and SWE is the initial one [Eq. (2)]. During ablation, the SCF stays at full cover until SWE drops lower than  $W_{\text{melt}}$ , at which point there is a more

gradual reduction in SCF as in Fig. 3. The SCF is then calculated as follows:

$$F = \begin{cases} \min\left(\frac{W}{W_{\min}}, 1\right) & \text{if } dW \geq 0 \\ \min\left(\frac{W}{W_{\text{melt}}}, 1\right) & \text{if } dW < 0 \end{cases}, \quad (3)$$

where  $dW$  is the variation of SWE between two time steps and  $W_{\text{melt}}$  is the new parameter characterizing the ablation part of the curve. It should depend on terrain aspect and topography, thus being catchment-specific, but it was defined empirically in this study (see section 5d). Because of melt events occurring when accumulation prevails, conditions related to the variation in SWE were added to prevent a substantial decrease of the SCF when melt events are small. Note also that the melting rate is assumed to be uniform in each catchment unit. This is not a limitation because the spatial distribution of the melting rate can be refined by decreasing the catchment size.

#### 4. Application to the Durance watershed

##### a. Topographic indices and surface parameters

The 25-m DEM was also used to calculate the topographic indices. Their minimum values in the upper Durance River region are lower than in catchments located downstream, indicating that the slopes are steeper. This is in good agreement with Table 1, which shows a high degree of topographic variability within each catchment in this region.

Vegetation parameters (LAI, albedo, roughness length, and soil depth) were extracted from the ECOCLIMAP database. In addition to forests, grassland, and bare soil, a small proportion of glacier remains in the upper Durance watershed, according to ECOCLIMAP (2.5%), but it is not taken into account in the CLSM. From the fractions of sand and clay provided by ECOCLIMAP, soil texture was defined using the U.S. Department of Agriculture triangle from which soil parameters such as porosity, hydraulic conductivity, matric potential at saturation, and wilting point were deduced following the values of Cosby et al. (1984).

##### b. Meteorological data

The système d'analyse fournissant des renseignements atmosphériques à la neige (SAFRAN), a mesoscale atmospheric reanalysis over France (Quintana-Seguí et al. 2008; Vidal et al. 2010), provides the seven meteorological forcings needed by the CLSM at an hourly time step and on a 8-km grid: rainfall (rain) and snowfall (snow),

incoming longwave and shortwave radiation (LW↓ and SW↓), air temperature ( $T$ ) and humidity ( $Q$ ) at 2 m, and wind speed ( $V$ ) at 10 m. However, SAFRAN underestimates precipitation, especially snowfall (Lafayssé 2011). This could be explained by the scarcity of meteorological stations at high altitudes and a poor capture of snowflakes by rain gauges. Spatialisation des précipitations en Zone de Montagne (SPAZM) is another meteorological reanalysis recently elaborated for the French mountains (Gottardi 2009). This new analysis uses more ground observations and a statistical approach that accounts for the orographic effect on precipitation based on weather patterns. Precipitation is 27% higher in SPAZM than in SAFRAN, and the difference in precipitation can reach 70% in the Massif des Écrins (northwest of the watershed) where snowfall is dominant. In addition to being more realistic, this dataset has a finer resolution than SAFRAN because it provides information on a 1-km grid. However, only daily mean temperatures and precipitation are given.

A hybridization of SAFRAN and SPAZM was performed to take advantage of the two datasets whose characteristics are summarized in Table 2. It consists of correcting and downscaling SAFRAN data based on SPAZM monthly mean temperatures and precipitation totals, using a method similar to that of Sheffield et al. (2006). Biases of precipitation in SAFRAN were first removed by scaling the hourly values so that their monthly totals match those of SPAZM:

$$P(x_{\text{sp}}, y_{\text{sp}}, h) = P_{\text{SAF}}(x_{\text{sa}}, y_{\text{sa}}, h) \frac{\sum P_{\text{SPAZM}}(x_{\text{sp}}, y_{\text{sp}})}{\sum P_{\text{SAF}}(x_{\text{sa}}, y_{\text{sa}})}, \quad (4)$$

where  $x_{\text{sp}}$  and  $y_{\text{sp}}$  are the 1-km SPAZM grid cell coordinates;  $x_{\text{sa}}$  and  $y_{\text{sa}}$  are the 8-km SAFRAN grid cell coordinates;  $h$  is the hour index; and  $\sum P_{\text{SPAZM}}$  and  $\sum P_{\text{SAF}}$  are the monthly SPAZM and SAFRAN precipitation totals, respectively.

The temperature data from SAFRAN were adjusted to match the SPAZM monthly values by shifting the SAFRAN hourly values by the difference between the SPAZM and the SAFRAN monthly means in accordance with

$$T(x_{\text{sp}}, y_{\text{sp}}, h) = T_{\text{SAF}}(x_{\text{sa}}, y_{\text{sa}}, h) + [\overline{T_{\text{SPAZM}}(x_{\text{sp}}, y_{\text{sp}})} - \overline{T_{\text{SAF}}(x_{\text{sa}}, y_{\text{sa}})}], \quad (5)$$

with  $\overline{T_{\text{SPAZM}}}$  and  $\overline{T_{\text{SAF}}}$  being the monthly air temperature means.

TABLE 2. Characteristics of meteorological datasets used in this study. Annual means of main variables are calculated over 1980–2009 for the upper Durance watershed.

Variables	SAFRAN $T$ , $Q$ , $V$ , rain, snow, LW↓ and SW↓	SPAZM $T_{\min}$ and $T_{\max}$ precipitation	DuO $T$ , $Q$ , $V$ , rain, snow, LW↓ and SW↓
Spatial resolution	8 km	1 km	1 km
Temporal resolution	Hourly	Daily	Hourly
Availability	1959–2010	1955–2010	1959–2010
References	Quintana-Seguí et al. (2008)	Gottardi et al. (2012)	—
	Annual means		
$T$ (°C)	3.4	4.5	4.5
Precipitation (mm yr <sup>-1</sup> )	1022	1300	1300
$Q$ (kg kg <sup>-1</sup> )	$4.43 \times 10^{-3}$	—	$4.82 \times 10^{-3}$
$V$ (m s <sup>-1</sup> )	1.7	—	1.7
LW↓ (W m <sup>-2</sup> )	268	—	272
SW↓ (W m <sup>-2</sup> )	174	—	174

To partition precipitation between rainfall and snowfall, a threshold air temperature was set to 1°C. This temperature is derived from Hingray et al. (2010), who defined an empirical relationship between the precipitation phase and the temperature using 17 stations located above 1000 m in the Swiss Alps. At this stage, temperature, snowfall, and rainfall were obtained on a 1-km grid and the mean elevation of the grid cell was extracted using the 25-m DEM. From these variables, assuming that relative humidity is held constant between the SAFRAN and the SPAZM grid cells to avoid the possibility of air supersaturation, we corrected specific humidity and incoming longwave radiation using the methods of Cosgrove et al. (2003) (see the appendix). The values of wind and incoming shortwave radiation on a SPAZM grid cell were kept equal to the values of the SAFRAN grid cell to which they belong.

The resulting reanalysis, an hourly dataset of seven meteorological variables on a 1-km grid, is called Durance Météo (DuO). Its characteristics are listed in Table 2. We verified that the daily distributions of precipitation and temperature between DuO and SPAZM as well as the ratio of snowfall–rainfall between DuO and SAFRAN are consistent. Using DuO meteorological forcing improved the simulations of the water budget, as it was shown in previous studies using other hybridized datasets (Ngo-Duc et al. 2005; Dirmeyer 2005; Guo et al. 2006; Weedon et al. 2011).

According to the DuO dataset, the upper Durance watershed receives approximately 1300 mm of precipitation per year, of which 48% is snowfall, and its mean temperature is about 4.5°C, with a range of –5° to 15°C in a year. Temperatures and precipitation are marked by an orographic effect, with temperatures being lower and precipitation greater in catchments at higher elevations. In addition to this orographic effect, precipitation is also influenced by the westerly general circulation over

France; catchments located in the western part of the upper Durance River watershed receive more precipitation than those located in the eastern part. Note that snowfall varies greatly from year to year: as an example, annual snowfall ranges from 250 to 850 mm yr<sup>-1</sup> in catchment 3.

### c. Two independent validation datasets

Simulated SCFs were validated using the observed SCFs derived from the MODIS images, as described in section 2a, and observed daily discharges provided by Électricité de France (EDF) were used to validate runoff simulations. There are six gauging stations in the upper Durance river watershed (Fig. 1, Table 1). Discharges at the watershed outlet, depicted in red in Fig. 1, were reconstructed; that is, the dam's influences were subtracted from observed discharges to reconstruct the discharges that would be observed without human disturbances. Because no routing procedure is included in the CLSM, we averaged the runoff of the upstream catchments over 10 days (a longer period than the residence time) to compare simulations with observations. Then, the spatially weighted average of runoff was calculated and the mean observed discharge over 10 days was converted into runoff.

Discharge observations show a nival regime with highly seasonal flows. The main peak flows occur in spring from April to June, with two low flow periods, one in winter during snow accumulation and another in summer when precipitation is low.

## 5. Results

### a. Modeling strategy

A set of numerical experiments (summarized in Table 3) was conducted with the CLSM to understand the impacts of different parameterizations on the water and energy

TABLE 3. Main characteristics of the studied simulations. Multitile configuration accounts for the different types of vegetation present in an elementary catchment according to ECOCLIMAP.

Simulation label	Snow parameterization	$W_{\min}$	$W_{\text{melt}}$	Vegetation
REF	Initial	13	—	Multitile
REF200	Initial	200	—	Multitile
REF400	Initial	400	—	Multitile
REF600	Initial	600	—	Multitile
REF <sub>forest</sub>	Initial	13	—	100% forest
REF <sub>grass</sub>	Initial	13	—	100% grassland
REF <sub>bs</sub>	Initial	13	—	100% bare soil
HYST	Hysteresis	13	Calibrated	Multitile
HYST <sub>forest</sub>	Hysteresis	13	Calibrated	100% forest
HYST <sub>grass</sub>	Hysteresis	13	Calibrated	100% grass
HYST <sub>bs</sub>	Hysteresis	13	Calibrated	100% bare soil

budgets. Two types of simulations were performed: the first type, called REF, with the initial configuration of the snow model, that is,  $W_{\text{melt}} = W_{\min}$ , and the second, called HYST, with the hysteresis in the SCF parameterization. The value of  $W_{\text{melt}}$  should depend on the terrain heterogeneities but was calibrated here by comparison with discharge observations to obtain the best performances using the relative bias and the Nash–Sutcliffe coefficient.

The influence of vegetation on snowpack dynamics was tested for both the REF and HYST versions. The catchments are either partitioned into different tiles of vegetation, referred to as multitile simulations, or covered with 100% of the same type of land cover, referred to as single-tile simulations (Table 3). REF200, REF400, and REF600 simulations were performed to test the sensitivity of the CLSM responses to  $W_{\min}$ .

Three hydrodynamic parameters related to the TOPMODEL concepts used in the CLSM were calibrated for the HYST simulation following Gascoïn et al. (2009a):  $K_0$ , the saturated hydraulic conductivity at the soil surface;  $\nu$ , characterizing the decay of the saturated hydraulic conductivity with depth; and  $D$ , the depth to bedrock. They were selected to give the best performances in terms of runoff, low bias, and high Nash–Sutcliffe coefficient for simulation HYST. All the simulations mentioned above used the same set of hydrodynamic parameters. After initializing the CLSM for 3 yr, all simulations were run for 30 yr between August 1980 and July 2009.

### b. Initial snow-cover parameterization

The REF simulation allows the coexistence of three types of land cover—forests, grassland, and bare soil (see Table 1)—within an elementary catchment via the “mosaic” approach adopted in this study (section 3b). Figure 6 shows that the duration of snow cover and the maximum SWE strongly depends on the land cover. The snowpack dynamics will indeed depend on vegetation via

two parameters, albedo and vegetation roughness length. The albedo of the SCF is reduced by a snow-masking depth depending on the vegetation type (Hansen et al. 1983). Evaporation and sublimation are enhanced by turbulent fluxes (Brutsaert 2005) so that more sublimation is produced over vegetation with high roughness length (i.e., small aerodynamic resistance) than over vegetation with low roughness length. Because of these two parameters, the development and duration of the snowpack are different from tile to tile with identical meteorological forcings.

The shape of the SCD initially implemented in the snow model (Fig. 5a) is recognizable in the single-tile simulations (REF<sub>forest</sub>, REF<sub>grass</sub>, and REF<sub>bs</sub> in Figs. 6b–d), but it is not recognizable in the REF simulation using a multitile configuration (Fig. 6). The combination of different vegetation tiles, each influencing the snowpack dynamics differently, leads to a vegetation-driven hysteresis in the SCD at the catchment scale (Fig. 6a). Nevertheless, the ablation part of this curve is mostly parallel to the accumulation part, while the analysis of MODIS data (Figs. 2–4) suggests that the slopes of the two branches should differ more.

In terms of runoff, the REF simulation gives a good runoff volume with relative biases ranging from  $-5\%$  to  $8\%$  for all catchments, but it shows a peak discharge that starts too early and is sharper compared to the observed runoff as shown in red in Fig. 7a. The simulated snowpack seems to melt faster than the real one.

Nevertheless, SCFs from the REF simulation show good consistency with MODIS observations, as illustrated in Fig. 7b. The coefficient of correlation ( $r = 0.94$ ) calculated over 2000–09 between the simulated and observed maximum snow extent over 8 days confirms this result. Figure 7b also highlights a too sudden decrease in simulated SCFs when the snow melts, uncovering the catchment 2–3 weeks earlier than the more gradual decrease of observed SCFs. This early decrease

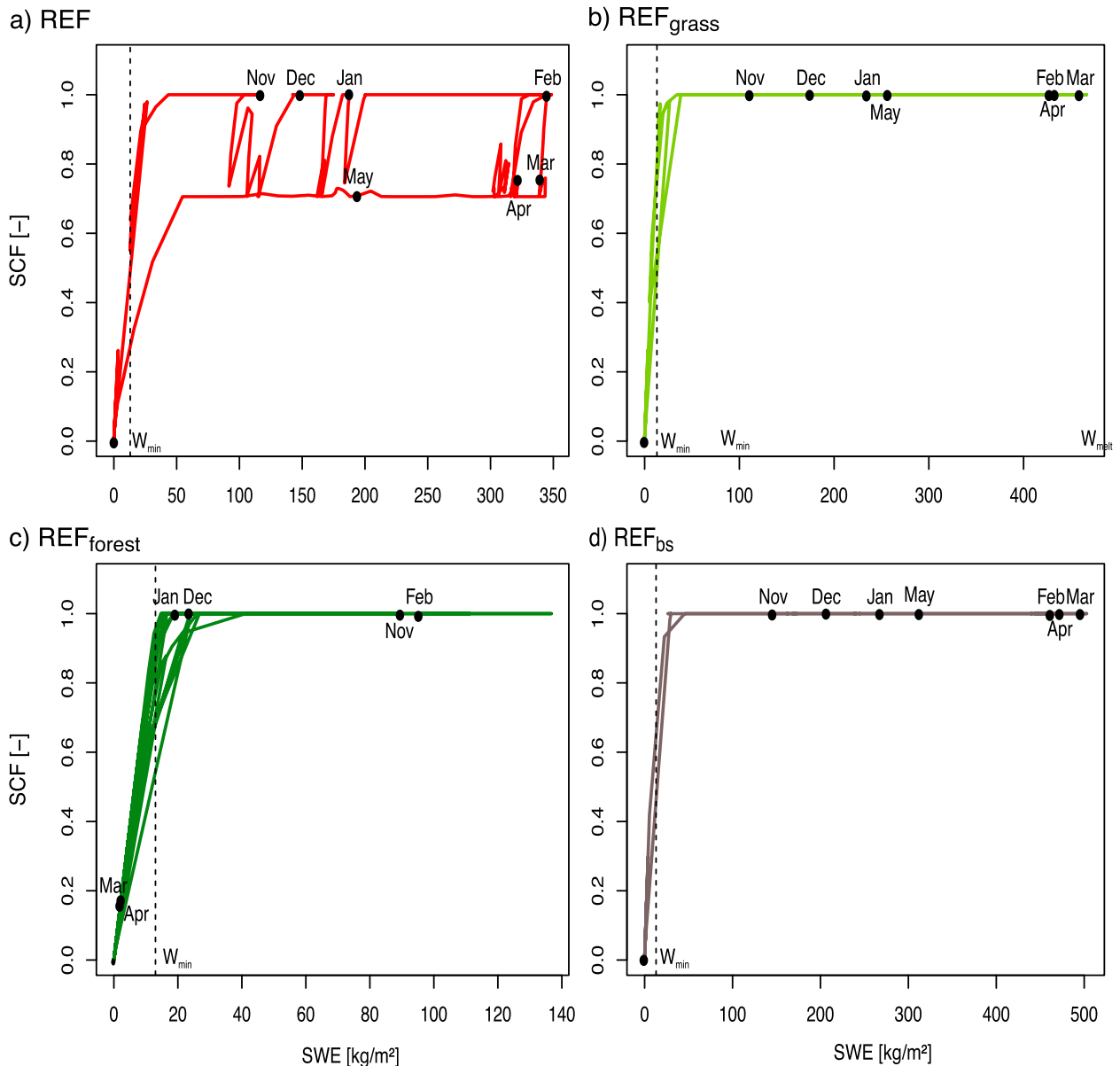


FIG. 6. Snow-cover depletion curves as a function of vegetation configuration in the CLSM for catchment 3 calculated from August 2003 and July 2004. (a) The REF simulation is for all the different types of vegetation in the catchment. (b) The  $REF_{grass}$ , (c)  $REF_{forest}$ , and (d)  $REF_{bs}$  are for 100% grassland, forest, and bare soil, respectively. The parameter  $W_{melt}$  in this catchment is equal to  $300 \text{ kg m}^{-2}$ .

in simulated SCFs is in good agreement with the lag previously noticed between observed and simulated runoff and supports the assumption that melting processes are not well represented in the CLSM.

### c. Sensitivity to $W_{min}$

To assess the influence of the SCF parameterization on snowpack dynamics and on the water budget, we tested the sensitivity of the runoff and the SCF simulation to  $W_{min}$  by increasing this parameter from 13 to 200, 400, and  $600 \text{ kg m}^{-2}$ . The value of  $W_{min}$  was recently increased by

Reichle et al. (2011) to  $26 \text{ kg m}^{-2}$  to improve the stability of the surface flux calculation when snow is present. Increasing  $W_{min}$  implies that more snow is needed on the catchment to obtain a full snow coverage. Figure 7a shows that increasing  $W_{min}$  delays and attenuates the peak discharge. The REF400 simulation is especially well synchronized with the observations, and Nash–Sutcliffe coefficients increase from 0.06 for the REF simulation to 0.47 for the REF400 simulation. The bias between observations and these two simulations, REF and REF400, tend to slightly decrease, but no significant change is found in the volume.

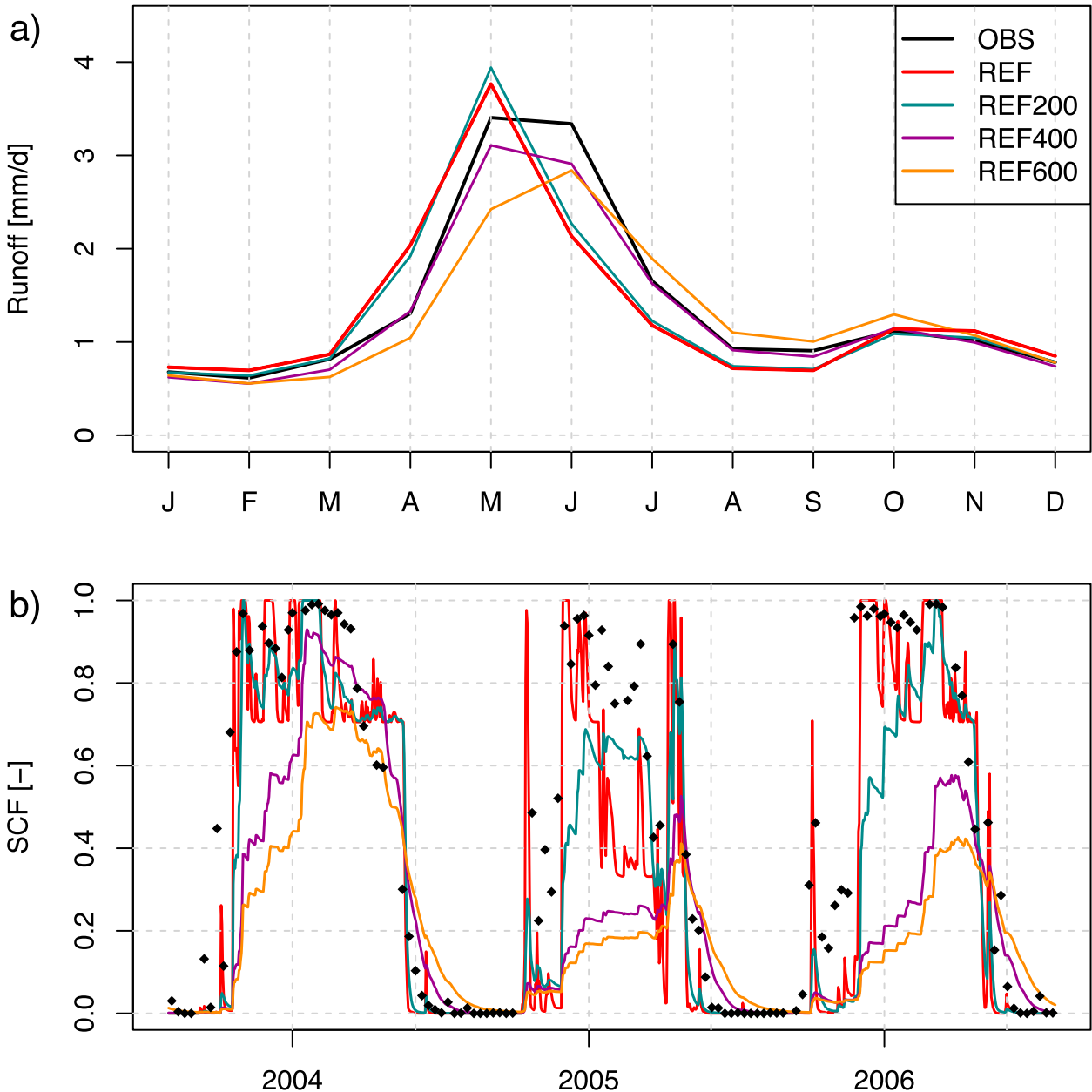


FIG. 7. (a) Annual hydrograph simulated by the different REFs compared with observations of the mean monthly values calculated from August 1980 to July 2009 in catchment 3 (colored and black lines, respectively). (b) Comparison between daily simulated SCFs (colored lines) and maximum SCFs observed (black diamonds) over 8 days from MODIS images.

Despite these improvements regarding the runoff simulation, simulations of SCFs with high  $W_{\min}$  are significantly deteriorated and are too small compared to the MODIS observations (Fig. 7b). As an example, SCFs from simulation REF600 with the highest  $W_{\min}$  never reach 100%, whereas observed SCFs do indicate full or almost full snow coverage of the catchment in winter. Correlation coefficients decrease from 0.88 when  $W_{\min} = 13$  to 0.47 when  $W_{\min} = 600$ . Yet, snow

stays longer in the catchment when increasing  $W_{\min}$ , which is consistent with the observations. Simulation REF400, in which runoff is well phased compared to the observed peak discharge, captures the melting part of the SCFs' evolution fairly well. These results show that increasing  $W_{\min}$  does have an effect on the snowmelt process and improves the runoff simulation, but this is at the expense of the SCFs simulation that underestimates the observations.

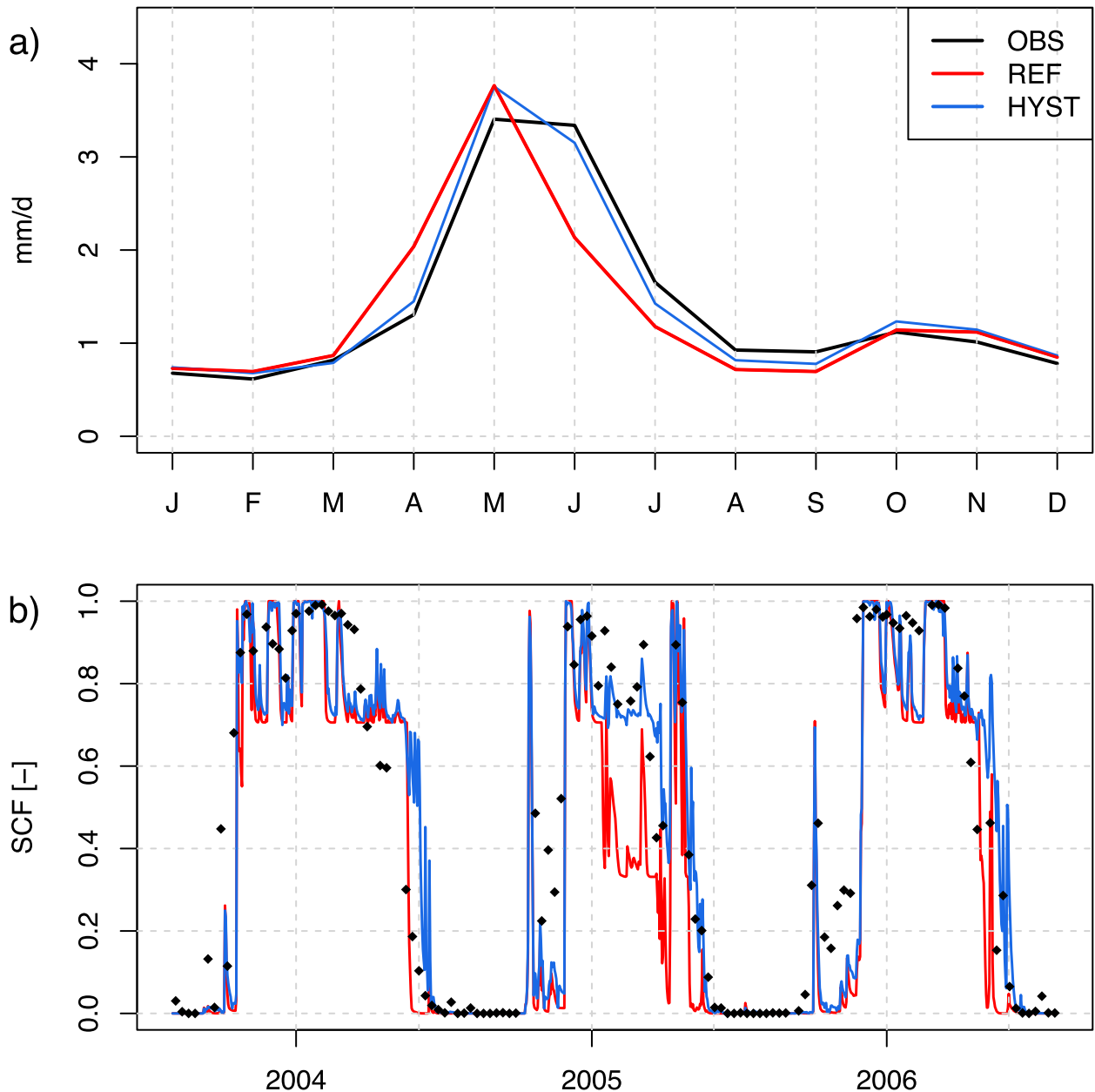


FIG. 8. (a) Comparison of annual hydrographs between observed (black) and simulations REF (red) and HYST (blue) for 1980–2009 in catchment 3. (b) Comparison of SCF evolution between the same simulations and observations.

#### d. Introducing the hysteresis in the SCF parameterization

The melt is not well simulated with the initial snow-cover parameterization; this is likely because factors other than vegetation, such as slopes and aspect, influence the evolution of the snow-cover extent. Implementing the hysteresis in the SCD allows these factors to be taken into account. Table 1 shows the different values of  $W_{\text{melt}}$  calibrated for each catchment. As expected, the

upstream catchments most influenced by snow have higher  $W_{\text{melt}}$ . Figure 8a shows an improvement in the peak discharge timing and rate between REF and HYST. The peak discharge of the HYST simulation starts later, lasts longer, and is thus closer to the observed peak discharge.

Considering all gauged catchments, Fig. 9 shows how closely the runoff and SCF simulations REF and HYST match their respective observations (discharge at the six gauging stations and MODIS images). The correlation

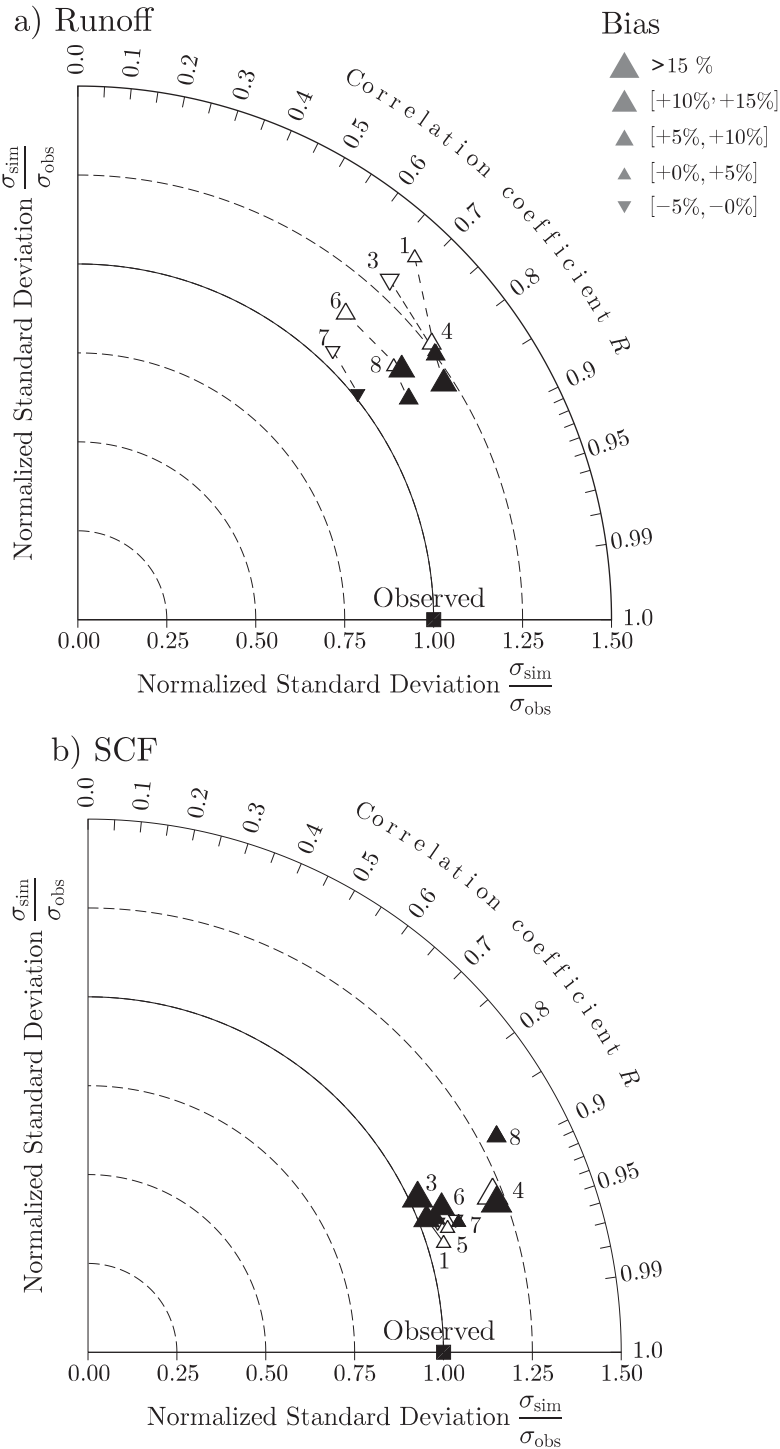


FIG. 9. Taylor diagrams (Taylor 2001) showing the performances of simulations REF (empty triangles) and HYST (filled triangles) for the six gauge stations in the upper Durance watershed of (a) 10-day averaged runoff and (b) maximum snow extent over 8 days compared to the MODIS images. The black square shows the location of the observations in the Taylor space. The distance between the simulation locations (triangles) and the reference point (black square) represents the RMSE of the centered time series. The magnitude of relative biases is depicted by the size and direction of the triangles with the catchment numbers indicated above the triangles.

coefficients for runoff simulations increase from REF to HYST without deteriorating the normalized standard deviation, reflecting the amplitude of the time series. Therefore, Fig. 9 confirms that the dynamics of melt are getting better for all gauged catchments of the upper Durance. Besides, the bias remains within a satisfactory range of values, although it slightly increases from REF to HYST. Concerning the SCF simulations, no significant difference between simulations REF and HYST is shown, either in terms of dynamics (empty and full triangles are more or less superimposed) or in terms of volume (similar bias). As a consequence, the new SCF parameterization leads to a more realistic runoff simulation in all the studied catchments without a significant deterioration of the SCF simulation.

In general, the introduction of the hysteresis maintains more snow over the catchment during a longer period. The maximum SWE over the catchment is on average 25% more important in the HYST simulation than in the REF simulation, and the snow-covered period lasts an average of 10 days longer (Table 4). At the end of spring, the SCFs are sometimes overestimated by the HYST simulation, as illustrated in Fig. 8b for 2003–04, leading to a slight increase of the RMSE from REF to HYST.

Yet, on average, the coefficients of correlation remain around 0.9 for all catchments and become variable when computed over individual years (Table 4). MODIS observations are better reproduced by the HYST simulation than by the REF simulation when the amount of snowfall is low as in 2004–05. The annual snowfall is 35% smaller than the mean amount over 2000–10; 40% of the snowfall occurs between October and January, then almost no snowfall from January to March, and an important snowfall event in April accounting for 46% of the total amount of snowfall. The low snowfall between January and March can be seen in Fig. 8b in the observations and in both simulations. This period of low snowfall is better simulated by HYST with an SCF of 70% maintained over the catchment, whereas REF strongly underestimates the snow-cover extent. The high frequency of SCF values of 70% in the two simulations, REF and HYST, especially at the end of the snow season in 2003–04 and in 2005–06, is due to the faster disappearance of snow over forests, as explained in section 5b.

The hysteresis implemented in the SCD modifies the evolution of the SCF and, thus, the energy budget. The increased duration of snow cover leads to a decrease of net radiation (–8%) (more upward radiation), thus reducing the energy available for the turbulent fluxes. As a result, the mean surface temperature decreases by 0.8°C. The increased duration of snow cover also leads to decreased transpiration and evaporation from bare soil

TABLE 4. Comparison of the REF and HYST simulations and MODIS observations (OBS) for the end of the snow-covered period, maximum annual SWE, and the correlation coefficient calculated for every year from August 2000 to July 2009 in catchment 3.

Year	DOY < 5%			Max SWE (kg m <sup>-2</sup> )		r <sup>2</sup>	
	OBS	REF	HYST	REF	HYST	REF	HYST
2000–01	314	298	314	535	527	0.86	0.84
2001–02	298	306	306	99	124	0.92	0.94
2002–03	290	290	298	267	267	0.85	0.80
2003–04	305	313	313	348	359	0.92	0.85
2004–05	298	290	290	69	97	0.83	0.89
2005–06	306	282	306	181	186	0.91	0.88
2006–07	298	306	306	63	146	0.90	0.91
2007–08	313	289	313	193	226	0.93	0.94
2008–09	322	290	322	369	376	0.89	0.87

(–2% and –9%, respectively) by preventing transpiration from the vegetation and evaporation from bare soil. The increase of the mean SWE is caused by the increased duration of the snow cover and a slight decrease in sublimation (–2%). The decrease of these components of evapotranspiration leads to an increase in runoff (Fig. 9). Both energy and water budgets are therefore impacted by the new SCF parameterization.

## 6. Discussion

To assess the impacts of the SCF parameterization with hysteresis on each type of land cover and their contribution to the changes noted at the catchment scale, we performed three other simulations of type HYST accounting for only one type of land cover (Table 3) as we did for type REF in the previous section. Figure 10 shows that changes between REF and HYST over bare soil and grassland are in the same direction and contribute the most to the changes of the multitype simulation HYST. In contrast, the changes over forests are very small and the introduction of the hysteresis does not really impact the evolution of the snowpack. This could be explained by the fact that an important difference between the three types of land cover is the repartition of snowpack ablation between melt and sublimation. Over forested areas (mainly needleleaf), sublimation losses are important and account on average for 250 mm yr<sup>-1</sup> in the upper Durance watershed, that is, 45% of the snow-cover ablation is in good agreement with Lundberg et al. (1998) and Pomeroy et al. (1998). In contrast, sublimation losses account only for 4% and 7% of the snowpack ablation over bare soil and grassland, respectively.

The parameter  $W_{\text{melt}}$  was introduced to strengthen the hysteresis of the SCD at the catchment scale and is likely to account for the influence of topography and aspect on

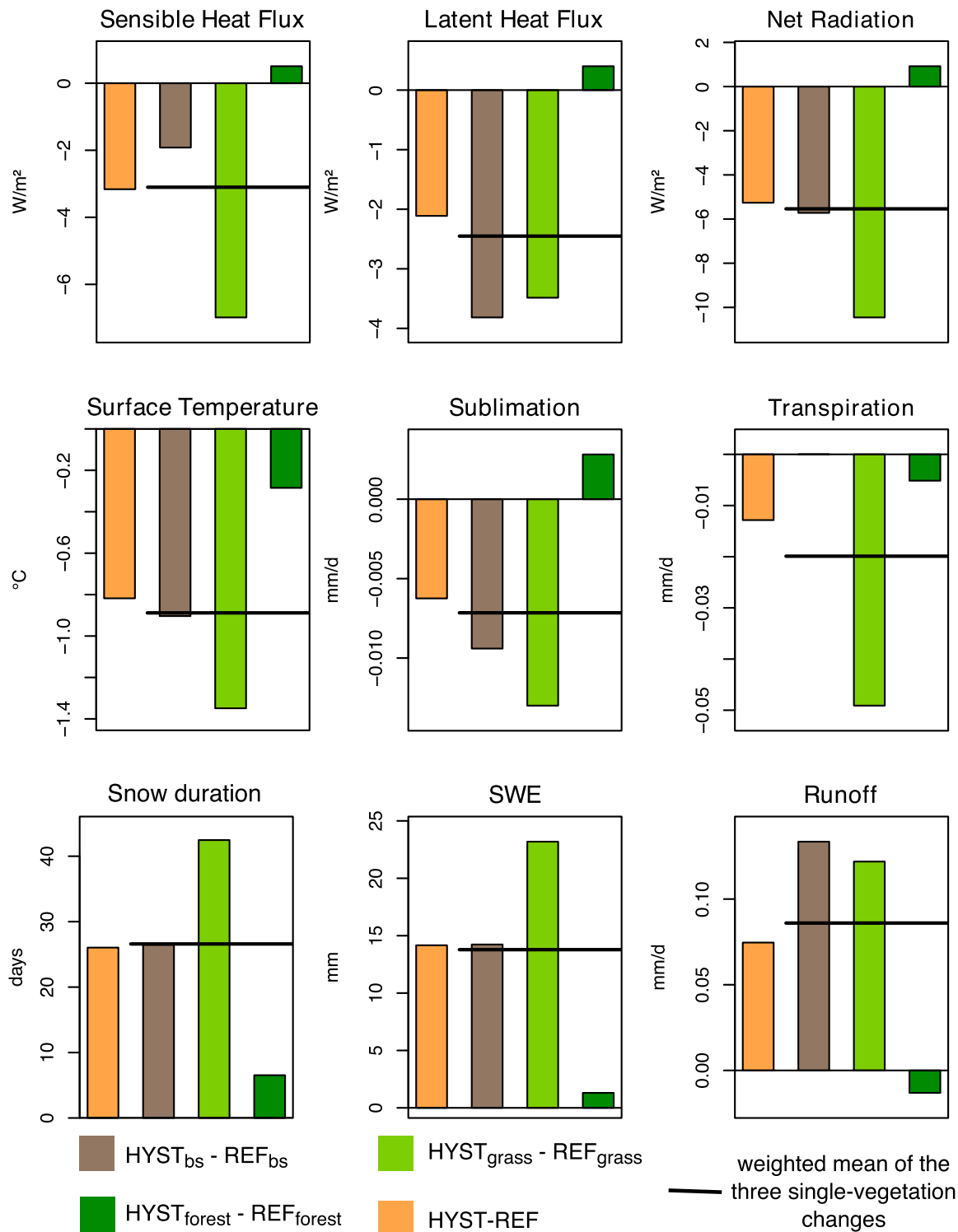


FIG. 10. Changes in energy and hydrological variables (listed above each panel) caused by a hysteresis SCD in catchment 3 over 1980–2009. Changes between the simulations HYST and REF are depicted by orange bars. The other three bars (gray, and light and dark green) show the changes between the single-tile HYST and REF simulations. The black line represents the surface weighted mean of the three single-vegetation changes.

the melting process. It is therefore normal that the impacts of the SCF parameterization with hysteresis are more important in tiles where melt is the dominant ablation process. Moreover, [Ellis et al. \(2013\)](#) showed that the effect of aspect (north or south facing) on melt is less important in forests than in open landscapes such as bare soil or grassland. This is again consistent with the fact that forested areas are not impacted by the introduction of the hysteresis in the SCF parameterization. In [section 5d](#), we demonstrated that the parameter  $W_{\text{melt}}$  does change the dynamics of the melt, but does not significantly change the sublimation losses (only  $-2\%$ ), and thus maintains the same repartition between melt and sublimation in terms of volume.

The multitile configuration and the parameter  $W_{\text{melt}}$  represent two types of subgrid variability that do not influence the snowpack in the same way. The multitile configuration is mainly related to the subgrid sublimation variability, a process that occurs throughout the snow season, especially at its beginning ([Hood et al. 1999](#)), whereas the parameter  $W_{\text{melt}}$  is related to the melt occurring mainly at the end of the snow season. Note that sublimation contributes to 18% of the snow-cover ablation using the multitile simulation HYST and that this is consistent with the values reported for mid-latitude Alpine catchments, ranging between 15% and 20% ([Kattelmann and Elder 1991](#); [Marks et al. 1992](#); [Hood et al. 1999](#)).

## 7. Conclusions

In this article, we first highlighted the differences in dynamics between accumulation and depletion of the snow cover in the Alps using MODIS snow-cover extent images. Indeed, we demonstrated that the SCF increases faster than it decreases. The use of snow-depth measurements allowed us to confirm that the difference between SCF accumulation and ablation rates is due to the existence of a hysteresis in the SCD at the catchment scale, as [Swenson and Lawrence \(2012\)](#) and [Luce et al. \(1999\)](#) highlighted in other environments. We then applied the CLSM in the upper Durance watershed. Although, the initial snow-cover parameterization of the CLSM captures the overall evolution of the SCFs fairly well, it cannot reproduce the melting period. The catchment is uncovered a few weeks earlier than in the MODIS observations, and the spring thaw is not well simulated.

We demonstrated the efficiency of introducing a hysteresis in the SCD to correctly simulate melting events and the dynamics of snow-cover extent. This led to a great improvement in reproducing the timing and shape of the spring thaw. It also increased the duration

of the snow cover in agreement with the MODIS observations and improved the simulation of the SCF evolution in years with a small amount of snowfall. This is important given that less snow is expected in these regions because of climate change.

However, we noted an overestimation of the simulated SCFs compared to MODIS images at the end of spring. This may be related to a shortcoming of the model in which the snow depth is assumed to be uniform. Hence, when snow falls on a heterogeneous snow cover ( $\text{SCF} < 1$ ), the resulting SWE is uniformly redistributed, leading to stronger insulation, and thus lower surface temperatures during snowmelt, than if the memory of heterogeneous snow depths was kept. It is noteworthy that the resulting snow-depth heterogeneities can be enhanced by the so-called windblown effect, which leads to redistributing snow and increasing sublimation, especially at high altitudes, where wind speed is high ([Liston 2004](#); [Strasser et al. 2008](#); [Gascoïn et al. 2012](#)). Two strategies could be explored to solve this problem, either by using the CLSM at a much higher resolution or by introducing a statistical distribution of snow depth within the elementary catchments following ([Liston 2004](#)). Part of the discrepancies between the model and the observations may also be due to the lack of explicit representation of the snow/vegetation interactions in the CLSM snow scheme, especially in forested zones ([Rutter et al. 2009](#)).

Anyway, the new snow-cover parameterization introduced in this paper allowed us to get a satisfactory simulation of both runoff and snow-cover extent without increasing the computational load. The parameter  $W_{\text{melt}}$  was calibrated for simplicity, but it should depend on morphological features of the catchment, such as mean elevation, elevation range, terrain roughness, or hillslope orientation. A generic application of the parameterization would thus require us to find a relationship between these morphological parameters and  $W_{\text{melt}}$ , which might benefit from the use of hydrological catchment as elementary land surface units in the CLSM. The combination of such a relationship with the physically based snow description and the multitile configuration of the CLSM would then offer an approach that is flexible enough to account for various impacts of global change on snow dynamics and water resources in Alpine environments, from climate change to land cover change.

*Acknowledgments.* This work has been carried out in the framework of the project R<sup>2</sup>D<sup>2</sup>-2050 supported by the program Gestion et Impact du Changement Climatique de le Ministère de l'Écologie, du Développement Durable et de l'Énergie. Claire Magand was supported by

a grant from l'Agence de l'Eau Rhône Méditerranée Corse. Simon Gascoin was supported by Fondcyt Chile (Grant 11090445). The authors are grateful for the meteorological data from the SAFRAN database provided by Météo-France and from the SPAZM database provided by Frederic Gottardi of Électricité de France. We also wish to thank Thibault Mathevet of Électricité de France for providing us with naturalized flows.

## APPENDIX

### Equations for Meteorological Dataset Construction

#### a. Air pressure

Surface air pressure is determined from elevation using

$$P(z) = P_0 \exp\left(-\frac{gM_a}{RT}z\right), \quad (\text{A1})$$

where  $P_0$  is the surface air pressure at sea level (Pa),  $g$  is the gravitational constant ( $\text{m s}^{-2}$ ),  $M_a$  is the air molar mass ( $\text{kg mol}^{-1}$ ),  $R$  is the gas constant ( $\text{J K}^{-1} \text{mol}^{-1}$ ), and  $T$  is the air temperature (K). The temperature is considered equal to  $15^\circ\text{C}$  (Allen et al. 1998).

#### b. Air specific humidity

It is important to modify specific humidity when changing air temperature to avoid the possibility of super saturation. Like Cosgrove et al. (2003), we assume that the relative humidity is held constant between the SAFRAN and the SPAZM grid cells.

$$\text{RH} = \left[ \frac{q(z_{\text{sp}}, t)}{q_{\text{sat}}(z_{\text{sp}}, t)} \right] 100 = \left[ \frac{q(z_{\text{sa}}, t)}{q_{\text{sat}}(z_{\text{sa}}, t)} \right] 100, \quad (\text{A2})$$

where  $z_{\text{sa}}$  is the elevation of the SAFRAN grid cell and  $z_{\text{sp}}$  is the elevation of the SPAZM grid cell. The specific humidity in the SPAZM cell is calculated from Eq. (A2) and from the value given by SAFRAN.

The specific humidity at saturation  $q_{\text{sat}}$  is then calculated as follows:

$$q_{\text{sat}} = \frac{0.622e_s}{P - 0.378e_s}, \quad (\text{A3})$$

where  $e_s$  is the vapor pressure (hPa).

There are many empirical equations to determine vapor pressure; the one we use comes from the reference report about evapotranspiration written by Allen et al. (1998):

$$e_s = 6.108 \exp\left[\frac{17.27(T - 273.15)}{(T - 273.15) + 237.3}\right]. \quad (\text{A4})$$

#### c. Incident longwave radiation

Incident longwave radiation  $\text{IR}\downarrow$  is described by the Stefan–Boltzmann law. Brutsaert (1982) simplifies this equation as follows:

$$\text{IR}\downarrow = \epsilon_{\text{ac}} \sigma T_a^4, \quad (\text{A5})$$

where  $\sigma$  is the Stefan–Boltzmann constant, equal to  $5.6704 \times 10^{-8} \text{ W m}^{-2} \text{ K}^{-4}$ ;  $T_a$  is the air temperature (K); and  $\epsilon_{\text{ac}}$  is atmospheric emissivity under clear skies, estimated using

$$\epsilon_{\text{ac}} = 1.24 \left(\frac{e_a}{T_a}\right)^{1/7}. \quad (\text{A6})$$

In this equation,  $e_a$  is the vapor pressure (mb) equal to

$$e_a = \frac{qP}{\zeta}, \quad (\text{A7})$$

with  $q$  being the specific air humidity,  $P$  being the surface air pressure, and  $\zeta$  being the ratio between the water and air molar masses. We assumed that the variation of emissivity with elevation is similar whether the sky is clear or clouded:

$$\frac{\epsilon_{\text{ac}}(z_{\text{sp}})}{\epsilon_{\text{ac}}(z_{\text{sa}})} = \frac{\epsilon_n(z_{\text{sp}})}{\epsilon_n(z_{\text{sa}})}, \quad (\text{A8})$$

where  $\epsilon_n$  is the emissivity accounting for cloudiness.

By combining the equations listed above, the incident longwave radiation is calculated according to the following equation:

$$\text{IR}\downarrow(z_{\text{sp}}, t) = \left\{ \frac{\text{IR}\downarrow(z_{\text{sa}}, t)}{\sigma T(z_{\text{sa}}, t)^4} \left[ \frac{q(z_{\text{sp}}, t)P(z_{\text{sp}})T(z_{\text{sa}}, t)}{q(z_{\text{sa}}, t)P(z_{\text{sa}})T(z_{\text{sp}}, t)} \right]^{1/7} \right\} \sigma T(z_{\text{sp}}, t)^4. \quad (\text{A9})$$

## REFERENCES

- Allen, R., L. Pereira, D. Raes, and M. Smith, 1998: Crop evapotranspiration: Guidelines for computing crop water requirements. FAO Irrigation and Drainage Paper 56, FAO, 328 pp.
- Beven, K., and M. Kirkby, 1979: A physically based, variable contributing area model of basin hydrology/un modèle à base physique de zone d'appel variable de l'hydrologie du bassin versant. *Hydrol. Sci. J.*, **24**, 43–69, doi:10.1080/02626667909491834.
- Boone, A., and P. Etchevers, 2001: An intercomparison of three snow schemes of varying complexity coupled to the same land surface model: Local-scale evaluation at an Alpine site. *J. Hydrometeorol.*, **2**, 374–394, doi:10.1175/1525-7541(2001)002<0374:AIOTSS>2.0.CO;2.
- Brutsaert, W., 1982: *Evaporation into the Atmosphere: Theory, History, and Applications*. Vol. 1. Springer, 299 pp.
- , 2005: *Hydrology: An Introduction*. Cambridge University Press, 605 pp.
- Cosby, B., G. Hornberger, R. Clapp, and T. Ginn, 1984: A statistical exploration of the relationships of soil moisture characteristics to the physical properties of soils. *Water Resour. Res.*, **20**, 682–690, doi:10.1029/WR020i006p00682.
- Cosgrove, B., and Coauthors, 2003: Real-time and retrospective forcing in the North American Land Data Assimilation System (NLDAS) project. *J. Geophys. Res.*, **108**, 8842, doi:10.1029/2002JD003118.
- Déry, S., W. Crow, M. Stieglitz, and E. Wood, 2004: Modeling snow-cover heterogeneity over complex Arctic terrain for regional and global climate models. *J. Hydrometeorol.*, **5**, 33–48, doi:10.1175/1525-7541(2004)005<0033:MSHOCA>2.0.CO;2.
- Dirmeyer, P., 2005: The second Global Soil Wetness Project (GSWP-2): Multi-model analysis and implications for our perception of the land surface. COLA Tech. Rep. 185, Center for Ocean-Land-Atmosphere Studies, 44 pp. [Available online at [http://iges.org/pub/ctr/ctr\\_185.pdf](http://iges.org/pub/ctr/ctr_185.pdf).]
- Douville, H., J. Royer, and J. Mahfouf, 1995: A new snow parameterization for the Meteo-France climate model. *Climate Dyn.*, **12**, 21–35, doi:10.1007/BF00208760.
- Ducharne, A., R. Koster, M. Suarez, M. Stieglitz, and P. Kumar, 2000: A catchment-based approach to modeling land surface processes in a general circulation model: 2. Parameter estimation and model demonstration. *J. Geophys. Res.*, **105**, 24 823–24 838, doi:10.1029/2000JD900328.
- Dutra, E., G. Balsamo, P. Viterbo, P. M. Miranda, A. Beljaars, C. Schär, and K. Elder, 2010: An improved snow scheme for the ECMWF land surface model: Description and offline validation. *J. Hydrometeorol.*, **11**, 899–916, doi:10.1175/2010JHM1249.1.
- Ellis, C., J. Pomeroy, and T. Link, 2013: Modeling increases in snowmelt yield and desynchronization resulting from forest gap-thinning treatments in a northern mountain headwater basin. *Water Resour. Res.*, **49**, 936–949, doi:10.1002/wrcr.20089.
- Essery, R., and J. Pomeroy, 2004: Implications of spatial distributions of snow mass and melt rate for snow-cover depletion: Theoretical considerations. *Ann. Glaciol.*, **38**, 261–265, doi:10.3189/172756404781815275.
- Gascoïn, S., A. Ducharne, P. Ribstein, M. Carli, and F. Habets, 2009a: Adaptation of a catchment-based land surface model to the hydrogeological setting of the Somme River basin (France). *J. Hydrol.*, **368**, 105–116, doi:10.1016/j.jhydrol.2009.01.039.
- , —, —, Y. Lejeune, and P. Wagnon, 2009b: Dependence of bare soil albedo on soil moisture on the moraine of the Zongo Glacier (Bolivia): Implications for land surface modeling. *J. Geophys. Res.*, **114**, D19102, doi:10.1029/2009JD011709.
- , S. Lhermitte, C. Kinnard, K. Borstel, and G. E. Liston, 2012: Wind effects on snow cover in Pascua-Lama, Dry Andes of Chile. *Adv. Water Resour.*, **55**, 25–39, doi:10.1016/j.advwatres.2012.11.013.
- Gottardi, F., 2009: Estimation statistique et réanalyse des précipitations en montagne. Utilisation débauchées par types de temps et assimilation de données d'enneigement. Application aux grands massifs montagneux Français. Ph.D. thesis, Université Joseph Fourier, Grenoble/Institut National Polytechnique de Grenoble, 261 pp.
- , C. Obled, J. Gailhard, and E. Paquet, 2012: Statistical reanalysis of precipitation fields based on ground network data and weather patterns: Application over French mountains. *J. Hydrol.*, **432–433**, 154–167, doi:10.1016/j.jhydrol.2012.02.014.
- Gray, D., and D. Male, 1981: *Handbook of Snow: Principles, Processes, Management & Use*. Blackburn Press, 776 pp.
- Guo, Z., P. Dirmeyer, Z. Hu, X. Gao, and M. Zhao, 2006: Evaluation of the Second Global Soil Wetness Project soil moisture simulations: 2. Sensitivity to external meteorological forcing. *J. Geophys. Res.*, **111**, D22S03, doi:10.1029/2006JD007845.
- Hansen, J., G. Russell, D. Rind, P. Stone, A. Lacis, S. Lebedeff, R. Ruedy, and L. Travis, 1983: Efficient three-dimensional global models for climate studies: Models I and II. *Mon. Wea. Rev.*, **111**, 609–662, doi:10.1175/1520-0493(1983)111<0609:ETDGMF>2.0.CO;2.
- Hingray, B., B. Schaeffli, A. Mezghani, and Y. Hamdi, 2010: Signature-based model calibration for hydrological prediction in mesoscale alpine catchments. *Hydrol. Sci. J.*, **55**, 1002–1016, doi:10.1080/02626667.2010.505572.
- Hood, E., M. Williams, and D. Cline, 1999: Sublimation from a seasonal snowpack at a continental, mid-latitude alpine site. *Hydrol. Processes*, **13**, 1781–1797, doi:10.1002/(SICI)1099-1085(199909)13:12/13<1781::AID-HYP860>3.0.CO;2-C.
- Kattelmann, R., and K. Elder, 1991: Hydrologic characteristics and water balance of an alpine basin in the Sierra Nevada. *Water Resour. Res.*, **27**, 1553–1562, doi:10.1029/90WR02771.
- Koster, R., and M. Suarez, 1996: Energy and water balance calculations in the Mosaic LSM. NASA Tech. Memo. 104606, 70 pp.
- , —, A. Ducharne, M. Stieglitz, and P. Kumar, 2000: A catchment-based approach to modeling land surface processes in a general circulation model: 1. Model structure. *J. Geophys. Res.*, **105**, 24 809–24 822, doi:10.1029/2000JD900327.
- , S. P. Mahanama, B. Livneh, D. P. Lettenmaier, and R. H. Reichle, 2010: Skill in streamflow forecasts derived from large-scale estimates of soil moisture and snow. *Nat. Geosci.*, **3**, 613–616, doi:10.1038/ngeo944.
- Lafaysse, M., 2011: Changement climatique et régime hydrologique d'un bassin alpin. génération de scénarios sur la haute-durée, méthodologie d'évaluation et incertitudes associées. Ph.D. thesis, Université Paul Sabatier, 311 pp. [Available online at <http://thesesups.tlse.fr/1679/1/2011TOU30295.pdf>.]
- Liston, G., 2004: Representing subgrid snow cover heterogeneities in regional and global models. *J. Climate*, **17**, 1381–1397, doi:10.1175/1520-0442(2004)017<1381:RSSCHI>2.0.CO;2.
- Livneh, B., Y. Xia, K. E. Mitchell, M. B. Ek, and D. P. Lettenmaier, 2010: Noah LSM snow model diagnostics and enhancements. *J. Hydrometeorol.*, **11**, 721–738, doi:10.1175/2009JHM1174.1.
- Loth, B., and H. Graf, 1998: Modeling the snow cover in climate studies: 2. The sensitivity to internal snow parameters and

- interface processes. *J. Geophys. Res.*, **103**, 11 329–11 340, doi:10.1029/97JD01412.
- Luce, C. H., and D. G. Tarboton, 2004: The application of depletion curves for parameterization of subgrid variability of snow. *Hydrol. Processes*, **18**, 1409–1422, doi:10.1002/hyp.1420.
- , —, and K. R. Cooley, 1999: Sub-grid parameterization of snow distribution for an energy and mass balance snow cover model. *Hydrol. Processes*, **13**, 1921–1933, doi:10.1002/(SICI)1099-1085(199909)13:12/13<1921::AID-HYP867>3.0.CO;2-S.
- Lundberg, A., I. Calder, and R. Harding, 1998: Evaporation of intercepted snow: Measurement and modelling. *J. Hydrol.*, **206**, 151–163, doi:10.1016/S0022-1694(97)00016-4.
- Lynch-Stieglitz, M., 1994: The development and validation of a simple snow model for the GISS GCM. *J. Climate*, **7**, 1842–1855, doi:10.1175/1520-0442(1994)007<1842:TDAVOA>2.0.CO;2.
- Marks, D., J. Dozier, and R. E. Davis, 1992: Climate and energy exchange at the snow surface in the alpine region of the Sierra Nevada: 1. Meteorological measurements and monitoring. *Water Resour. Res.*, **28**, 3029–3042, doi:10.1029/92WR01482.
- Masson, V., J. Champeaux, F. Chauvin, C. Meriguet, and R. Lacaze, 2003: A global database of land surface parameters at 1-km resolution in meteorological and climate models. *J. Climate*, **16**, 1261–1282, doi:10.1175/1520-0442-16.9.1261.
- Mielke, A., and T. Roubicek, 2003: A rate-independent model for inelastic behavior of shape-memory alloys. *Multiscale Model. Simul.*, **1**, 571–597, doi:10.1137/S1540345903422860.
- Ngo-Duc, T., J. Polcher, and K. Laval, 2005: A 53-year forcing data set for land surface models. *J. Geophys. Res.*, **110**, D06116, doi:10.1029/2004JD005434.
- Niu, G., and Z. Yang, 2007: An observation-based formulation of snow cover fraction and its evaluation over large North American river basins. *J. Geophys. Res.*, **112**, D21101, doi:10.1029/2007JD008674.
- Parajka, J., and G. Blöschl, 2006: Validation of MODIS snow cover images over Austria. *Hydrol. Earth Syst. Sci. Discuss.*, **3**, 1569–1601, doi:10.5194/hessd-3-1569-2006.
- Picouet, C., 2012: Partie 3: Comparaison des données SWE (observations au sol) et SCA (MODIS) au droit des NRC. Tech. Rep., EDF-DTG, 18 pp.
- Pomeroy, J., D. Gray, K. Shook, B. Toth, R. Essery, A. Pietroniro, and N. Hedstrom, 1998: An evaluation of snow accumulation and ablation processes for land surface modelling. *Hydrol. Processes*, **12**, 2339–2367, doi:10.1002/(SICI)1099-1085(199812)12:15<2339::AID-HYP800>3.0.CO;2-L.
- Quintana-Seguí, P., and Coauthors, 2008: Analysis of near-surface atmospheric variables: Validation of the SAFRAN analysis over France. *J. Appl. Meteor. Climatol.*, **47**, 92–107, doi:10.1175/2007JAMC1636.1.
- Reichle, R., R. Koster, G. De Lannoy, B. Forman, Q. Liu, S. Mahanama, and A. Touré, 2011: Assessment and enhancement of MERRA land surface hydrology estimates. *J. Climate*, **24**, 6322–6338, doi:10.1175/JCLI-D-10-05033.1.
- Riggs, G. A., D. K. Hall, and V. V. Salomonson, 2006: MODIS snow products users' guide to Collection 5. Tech. Rep., NASA GSFC, 80 pp. [Available online at [http://modis-snow-ice.gsfc.nasa.gov/uploads/sug\\_c5.pdf](http://modis-snow-ice.gsfc.nasa.gov/uploads/sug_c5.pdf).]
- Roesch, A., M. Wild, H. Gilgen, and A. Ohmura, 2001: A new snow cover fraction parameterization for the ECHAM4 GCM. *Climate Dyn.*, **17**, 933–946, doi:10.1007/s003820100153.
- Rutter, N., and Coauthors, 2009: Evaluation of forest snow processes models (SnowMIP2). *J. Geophys. Res.*, **114**, D06111, doi:10.1029/2008JD011063.
- Sellers, P. J., and Coauthors, 1996: A revised land surface parameterization (SiB2) for atmospheric GCMs. Part I: Model formulation. *J. Climate*, **9**, 676–705, doi:10.1175/1520-0442(1996)009<0676:ARLSPF>2.0.CO;2.
- Sheffield, J., G. Goteti, and E. Wood, 2006: Development of a 50-yr high-resolution global dataset of meteorological forcings for land surface modeling. *J. Climate*, **19**, 3088–3111, doi:10.1175/JCLI3790.1.
- Slater, A. G., and Coauthors, 2001: The representation of snow in land surface schemes: Results from PILPS 2(d). *J. Hydrometeorol.*, **2**, 7–25, doi:10.1175/1525-7541(2001)002<0007:TROSIL>2.0.CO;2.
- Stieglitz, M., A. Ducharne, R. Koster, and M. Suarez, 2001: The impact of detailed snow physics on the simulation of snow cover and subsurface thermodynamics at continental scales. *J. Hydrometeorol.*, **2**, 228–242, doi:10.1175/1525-7541(2001)002<0228:TIODSP>2.0.CO;2.
- Strasser, U., M. Bernhardt, M. Weber, G. Liston, and W. Mauser, 2008: Is snow sublimation important in the alpine water balance? *The Cryosphere*, **2**, 53–66, doi:10.5194/tc-2-53-2008.
- Swenson, S., and D. Lawrence, 2012: A new fractional snow-covered area parameterization for the Community Land Model and its effect on the surface energy balance. *J. Geophys. Res.*, **117**, D21107, doi:10.1029/2012JD018178.
- Taylor, K. E., 2001: Summarizing multiple aspects of model performance in a single diagram. *J. Geophys. Res.*, **106**, 7183–7192, doi:10.1029/2000JD900719.
- Verseghy, D., 1991: Class—A Canadian land surface scheme for GCMs. I. Soil model. *Int. J. Climatol.*, **11**, 111–133, doi:10.1002/joc.3370110202.
- Vidal, J.-P., E. Martin, L. Franchistéguy, M. Baillon, and J.-M. Soubeyroux, 2010: A 50-year high-resolution atmospheric reanalysis over France with the SAFRAN system. *Int. J. Climatol.*, **30**, 1627–1644, doi:10.1002/joc.2003.
- Wang, T., 2012: Développement et évaluation du modèle de surface ORCHIDEE: Apport pour la simulation des cycles de l'eau et du carbone aux hautes latitudes. Ph.D. thesis, Université de Versailles Saint-Quentin-en-Yvelines, 320 pp.
- Weedon, G. P., and Coauthors, 2011: Creation of the WATCH forcing data and its use to assess global and regional reference crop evaporation over land during the twentieth century. *J. Hydrometeorol.*, **12**, 823–848, doi:10.1175/2011JHM1369.1.
- Yang, Z.-L., R. E. Dickinson, A. Robock, and K. Y. Vinnikov, 1997: Validation of the snow submodel of the biosphere-atmosphere transfer scheme with Russian snow cover and meteorological observational data. *J. Climate*, **10**, 353–373, doi:10.1175/1520-0442(1997)010<0353:VOTSSO>2.0.CO;2.